remote sensing

MDPI

Article

Global Leaf Chlorophyll Content Dataset (GLCC) from 2003–2012 to 2018–2020 Derived from MERIS and OLCI Satellite Data: Algorithm and Validation

Xiaojin Qian [1,2], Liangyun Liu [3,4,*], Xidong Chen [5], Xiao Zhang [3,4], Siyuan Chen [6] and Qi Sun [7]

[1] School of Geographic and Biologic Information, Nanjing University of Posts and Telecommunications, Nanjing 210023, China
[2] State Key Laboratory of Remote Sensing Science, Aerospace Information Research Institute, Chinese Academy of Sciences, Beijing 100101, China
[3] International Research Center of Big Data for Sustainable Development Goals, Beijing 100094, China
[4] Key Laboratory of Digital Earth Science, Aerospace Information Research Institute, Chinese Academy of Sciences, Beijing 100094, China
[5] College of Surveying and Geo-Informatics, North China University of Water Resources and Electric Power, Zhengzhou 450046, China
[6] College of Geological Engineering and Geomatics, Chang'an University, Xi'an 710054, China
[7] College of Surveying and Planning, Shangqiu Normal University, Shangqiu 476000, China
* Correspondence: liuly@radi.ac.cn

Abstract: Leaf chlorophyll content (LCC) is a prominent plant physiological trait and a proxy for leaf photosynthetic capacity. The acquisition of LCC data over large spatial and temporal scales facilitates vegetation growth monitoring and terrestrial carbon cycle modeling. In this study, a global 500 m LCC weekly dataset (GLCC) was produced from ENVISAT MERIS and Sentinel-3 OLCI satellite data using a physical radiative transfer modeling approach that considers the influence of canopy structure and soil background. Firstly, five look-up-tables (LUTs) were generated using PROSPECT-D+4-Scale and PROSAIL-D models for woody and non-woody plants. For the four LUTs applicable to woody plants, each LUT contains three sub-LUTs corresponding to three types of crown height. The one LUT applicable to non-woody vegetation type includes 25 sub-LUTs corresponding to five kinds of canopy structures and five kinds of soil backgrounds. The final retrieval was considered the aggregation of the LCC inversion results of all sub-LUTs for each plant function type (PFT). Then, the GLCC dataset was generated and validated using field measurements, yielding an overall accuracy of $R^2 = 0.41$ and RMSE = 8.94 $\mu g\ cm^{-2}$. Finally, the GLCC dataset presented acceptable consistency with the existing MERIS LCC dataset. OLCI, as the successor to MERIS data, was used for the first time to co-produce LCC data from 2003–2012 to 2018–2020 in conjunction with MERIS data. This new GLCC dataset spanning nearly 20 years will provide a valuable opportunity to analyze variations in vegetation dynamics.

Keywords: global mapping; leaf chlorophyll content; MERIS; OLCI

Citation: Qian, X.; Liu, L.; Chen, X.; Zhang, X.; Chen, S.; Sun, Q. Global Leaf Chlorophyll Content Dataset (GLCC) from 2003–2012 to 2018–2020 Derived from MERIS and OLCI Satellite Data: Algorithm and Validation. *Remote Sens.* **2023**, *15*, 700. https://doi.org/10.3390/rs15030700

Academic Editors: Xiaobin Guan and Jochem Verrelst

Received: 4 December 2022
Revised: 21 January 2023
Accepted: 22 January 2023
Published: 25 January 2023

1. Introduction

Carbon dioxide uptake by terrestrial plants through photosynthesis is the primary driver of multiple global biogeochemical cycles [1,2]. Therefore, quantifying photosynthesis on a global scale is fundamental to understanding the global carbon cycle [3]. Chlorophyll, as the primary photosynthetic pigment, facilitates the harvesting of energy from light and the conversion of the light energy into stored chemical energy, thus playing a vital role in the exchange of matter and energy fluxes [4,5]. Currently, many studies have indicated that leaf chlorophyll content (LCC) is closely related to plant photosynthetic capacity parameter (Vcmax) [6–10]. Moreover, leaf chlorophyll content has necessary implications on plant physiological status assessment and stress diagnosis [11–16]. As a result, deriving leaf chlorophyll content data over an extensive space and time is of great significance in reducing the uncertainty of terrestrial ecosystem productivity and carbon sink estimates [17].

Due to the heterogeneity of variations in LCC and the lack of observations that can detect these variations both spatially and temporally, it is impossible to monitor LCC on a global scale using ground-based observations [18]. Satellite-based remote sensing, through regular global measurements, has enabled continuous estimation of LCC [19,20]. The first global LCC dataset was generated using data from the ENVISAT MEdium Resolution Imaging Spectrometer (MERIS) based on the physical inversion method [21]. Recently, a neural network model has also been applied to generate a global LCC dataset from MERIS based on the PROSAIL model [22]. The 4SAIL model, which is designed for homogeneous canopies, may lead to higher uncertainties in LCC estimates in forest types. Moreover, MERIS is no longer in operation—it was in operation from 2003 to 2012. Although Moderate Resolution Imaging Spectroradiometer (MODIS) data have been used to produce a global LCC dataset for long time series, the lack of red-edge bands in MODIS data aggravates the uncertainty of retrievals [23]. As the successor of MERIS, Sentinel-3 Ocean and Land Colour Instrument (OLCI), also launched by the European Space Agency (ESA), will be used to continue the terrestrial vegetation monitoring mission.

Estimation of the leaf-scale parameter, LCC, from the canopy level remains challenging, as leaf scattering signals may be confounded with the signals of the canopy structure and soil background [24–29]. Varieties of vegetation indices (VIs) were developed and widely used to retrieve LCC due to their simplicity and high computational efficiency [30–33]. The development of VIs has gradually clarified the unique value of the red-edge bands and its reduced sensitivity to canopy structure and soil background has been considered [4,31,32,34–36]. While VI models may perform well at the field level, they usually cannot be applied to other species and regions due to the lack of a clear physical foundation, which depends heavily on the training samples [37,38]. In contrast, the physical models establish the relationships between the leaf optical properties and the vegetation spectra by simulating light interactions with the canopy based on radiative transfer theory. The radiative transfer model approach realizes a large number of vegetation leaf and canopy spectra simulations, which integrate a variety of confounding scene information, and is therefore considered ideal for global LCC mapping [5]. To manage the ill-posed problems in the inversion of crop LCC caused by the lack of prior information, a look-up-table (LUT) method that combines multiple types of canopy structure and soil background was proposed in our previous study [39]. However, the feasibility of this algorithm for the LCC estimation of other plant function types (PFTs) (e.g., forests and shrubs) is not yet known, nor is the applicability of this approach to OLCI satellite data.

This study aimed to generate a global LCC dataset using MERIS and OLCI data from 2003–2012 to 2018–2020 (GLCC) with an improved LUT approach by inverting radiative transfer models. Ground measurements covering six different PFTs were subsequently used to validate the LCC retrievals. In addition, this new LCC dataset was compared to the existing global LCC dataset to analyze its spatial and temporal characteristics. The global leaf chlorophyll content data spanning nearly two decades will contribute to vegetation dynamics monitoring and ecosystem modeling.

2. Data and Methods

2.1. Satellite Data

2.1.1. MERIS and OLCI Surface Reflectance Data

The MERIS full resolution surface reflectance (SR) and Sentinel-3 SY_2_SYN (synergy) products were selected for generating the global LCC product. The MERIS SR product was produced as a 7-day temporal synthesis from original images. It has 15 spectral bands ranging from the visible to the near-infrared with a resolution of 300 m. The SY_2_SYN product was launched by ESA in October 2018, and integrates the information from the OLCI and Land Surface Temperature Radiometer (SLSTR) on board ESA's Sentinel-3A and

Sentinel-3B satellites, including surface reflectance and aerosol parameters over land. OLCI has a 300 m resolution with 21 distinct bands. MERIS and OLCI surface reflectance was used to produce a global LCC dataset, mainly due to the possession of chlorophyll-sensitive red-edge bands, medium spatial resolution, and a short revisit cycle [40]. The band settings of MERIS and OLCI are shown in Table 1, and the ones in bold are used for LCC retrieval.

Table 1. The channel settings of MERIS and OLCI.

MERIS Channel	Center (nm)	Width (nm)	OLCI Channel	Center (nm)	Width (nm)
			Oa1	400	15
1	412.5	10	Oa2	412.5	10
2	442.5	10	Oa3	442.5	10
3	490	10	Oa4	490	10
4	510	10	Oa5	510	10
5	560	10	Oa6	560	10
6	620	10	Oa7	620	10
7	665	10	Oa8	665	10
			Oa9	673.75	7.5
8	**681.25**	**7.5**	**Oa10**	**681.25**	**7.5**
9	**708.75**	**10**	**Oa11**	**708.75**	**10**
10	**753.75**	**7.5**	**Oa12**	**753.75**	**7.5**
11	760.625	3.75	Oa13	761.25	2.5
			Oa14	764.375	3.75
			Oa15	767.5	2.5
12	778.75	15	Oa16	778.75	15
13	865	20	Oa17	865	20
14	885	10	Oa18	885	10
15	900	10	Oa19	900	10
			Oa20	940	20
			Oa21	1020	40

2.1.2. MODIS Land Cover Map

MODIS Land Cover Type (MCD12Q1) Version 6 provides global data with a 500 m spatial resolution at annual time steps from 2001 to 2020 (https://doi.org/10.5067/MODIS/MCD12Q1.006, accessed on January 2022). The International Geosphere Biosphere Programme (IGBP) scheme was used in this study, which has 17 land cover types, including 11 natural vegetation types. In this study, these 11 natural vegetation types were combined into the following 5 types: needleleaf forests, evergreen broadleaf forests, deciduous broadleaf forests, shrublands, and croplands/grasslands.

2.1.3. The Croft MERIS LCC Dataset

The 2003–2011 weekly global dataset of LCC was generated by Croft, et al. [21] (referred to as Croft MERIS LCC, hereafter) from MERIS data applying a two-step physical approach. For the first step, leaf reflectance was derived from the MERIS SR product using SAIL or 4-Scale canopy radiative transfer models based on the canopy structural characteristics. Secondly, the leaf chlorophyll content was inverted from the simulated leaf reflectance generated in the first step based on the PROSPECT-5 leaf radiative transfer model. The Croft MERIS LCC dataset with a 300 m spatial resolution was resampled at 500 m to facilitate the comparison with the GLCC dataset generated in this study.

2.2. LCC Field Measurements

The field LCC data covering six PFTs were collected to validate the GLCC dataset. The LCC data included 45 observations in deciduous broadleaf forests (DBF), 15 observations in evergreen broadleaf forests (EBF), 48 observations in needleleaf forests (ENF), 21 observations in grasslands (GRA), 29 observations in croplands (CRO), and 3 observations in shrublands (SHR). A significant source of these data is the National Ecological Observatory

Network (NEON), supported by the National Science Foundation (NSF) funded Grand Challenge project [41,42]. Based on Google Earth images, these sites are covered with relatively homogeneous vegetation at a 500 m scale. The number of samplings and dates for each ground measurement site are reported in Table 2. LCC measurement was carried out by laboratory chemical analysis. The statistical analyses of the field measured LCC data are shown in Table 3.

Table 2. Details of the field measurements of LCC for validation used in this study.

Site Name	Latitude	Longitude	PFT	Dominant Species	Sampling Date	Samples	Reference/Source
Sudbury_DBF	47.16	−81.71	DBF	Trembling aspen	Summer 2007	2	Simic, et al. [43]
Haliburton	45.24	−78.54	DBF	Sugar maple	May–September 2004	8	Zhang, et al. [44]
JERC_DBF	31.19	−84.47	DBF	Southern red oak	September 2019	7	National Ecological Observatory [45]
UNDE	46.23	−89.54	DBF	Red and sugar maple, aspen, paper birch	June 2019	8	
DELA	32.54	−87.81	DBF	Oak, hickory	April–May 2019	4	
CLBJ_DBF	33.40	−97.59	DBF	Post oak, blackjack oak	April–May 2019	13	
BONA	65.16	−147.54	DBF	—	July–August 2019	3	
SJER_EBF	37.11	−119.73	EBF	Evergreen oak	March–April 2019	8	
PUUM	19.56	−155.30	EBF	'Ohi'a lehua	January 2019	7	
Sudbury_Simic	47.18	−81.74	ENF	Black spruce	Summer 2007	5	Simic, et al. [43]
Sudbury_Zhang	47.16	−81.74	ENF	Black spruce	Summer 2003–2004	16	Zhang, et al. [29]
JERC_ENF	31.20	−84.46	ENF	Longleaf pine	September 2019	9	National Ecological Observatory [45]
NIWO_ENF	40.04	−105.56	ENF	lodgepole pine	August 2019	6	
WREF	45.83	−121.97	ENF	Douglas fir, western hemlock, pacific silver fir	July 2019	12	
CLBJ_GRA	33.37	−97.58	GRA	Bluestem	April–May 2019	6	
NIWO_GRA	40.05	−105.58	GRA	Curly sedge	August 2019	3	
SJER_GRA	37.10	−119.73	GRA	Bromus	March–April 2019	12	
US-Ne2	41.17	−96.47	CRO	Soybean	June–September 2004	21	University of Nebraska–Lincoln
KONA	39.13	−96.63	CRO	Wheat, corn	July 2019	8	National Ecological Observatory [45]
NIWO_SHR	40.05	−105.59	SHR	—	August 2019	1	
SJER_SHR	37.11	−119.75	SHR	Manzanita, whitethorn shrub	March–April 2019	2	

Table 3. Summary statistics of the field measured LCC (μg cm^{-2}).

PFT	Min	Max	Mean	SD	CV
DBF	18.44	63.46	38.94	9.39	0.24
EBF	16.14	53.38	34.08	11.60	0.34
ENF	20.57	56.28	33.04	7.35	0.22
GRA	15.94	57.49	32.73	11.59	0.35
CRO	12.06	64.88	39.30	13.64	0.35
SHR	19.43	35.40	29.51	7.16	0.24

Min, minimum value; Max, maximum value; SD, standard deviation; CV, coefficient of variation.

2.3. The Cross-Validation Sites

The site location information from the FLUXNET2015 dataset was extracted for the cross-validation between the Croft MERIS LCC dataset and the GLCC dataset. Considering the spatial-temporal consistency of satellite products, we selected 178 sites to validate the GLCC dataset in this study. The ground measurement sites in Table 2, the selected 178 cross-validation sites, and the IGBP land cover map are shown in Figure 1.

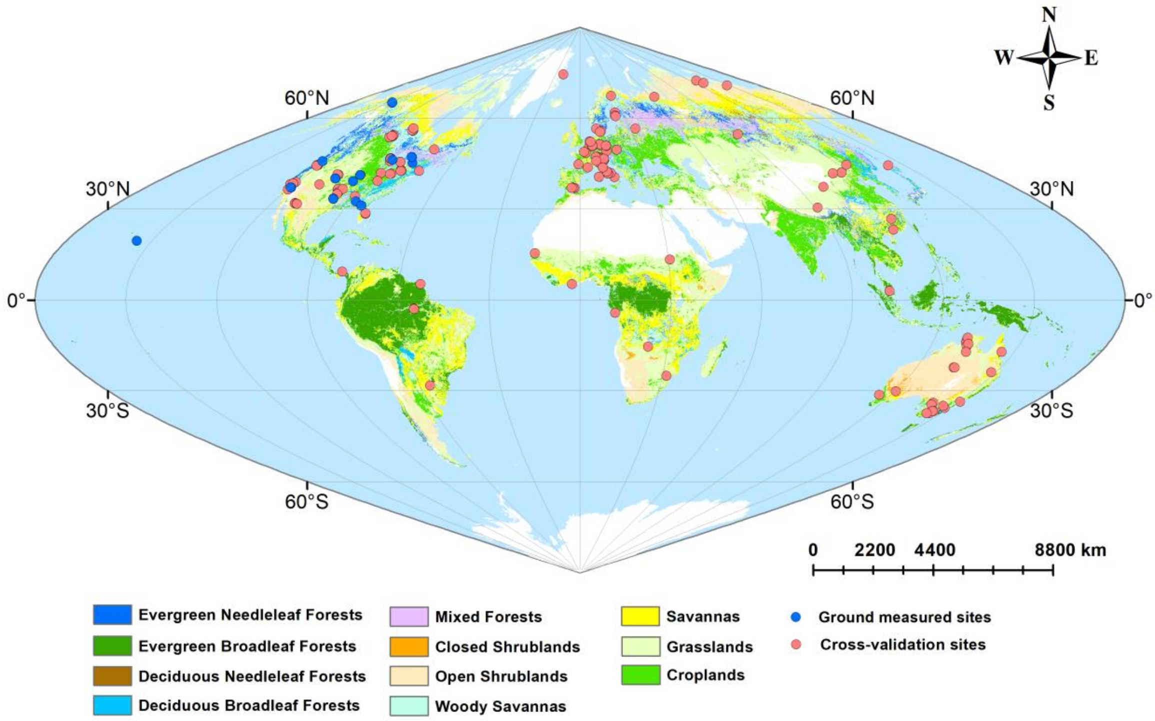

Figure 1. Global MCD12Q1 land cover map and the locations of the ground measurement sites and the cross-validation sites for validating the GLCC dataset.

2.4. Algorithm Development

An improved LUT approach was selected to derive LCC from satellite data on a global scale. For the first step, the 4SAIL canopy bidirectional reflectance model [46] and 4-Scale geometric-optical model [47] combined with the PROSPECT-D leaf optical properties model [48] were used to simulate the homogenous and heterogeneous canopy reflectance, respectively. Parameters used in the PROSPECT_D + 4SAIL(PROSAIL_D) and PROSPECT_D + 4-Scale models are listed in Table 4. Considering that canopy and soil are the main factors interfering with the inversion of leaf optical traits, an improved LUT inversion approach combined with multiple canopy structures and soil backgrounds was proposed to retrieve LCC. Crops and grasses are more susceptible to soil signals than woody plants; therefore, the canopy reflectance modeled by the PROSAIL_D model was divided into 25 groups based on five predefined kinds of canopy structure and five kinds of soil backgrounds, i.e., 25 sub-LUTs were constructed. The 25 sub-LUTs cover the majority of canopy structures and soil backgrounds for non-woody vegetation. Meanwhile, we grouped the canopy reflectance simulated by the 4-Scale models into three groups according to the pre-determined crown height, i.e., three sub-LUTs were constructed. Then, the red-edge bands indicated in Table 1 were directly applied to build a cost function in each sub-LUT. The final retrievals were obtained by fusing the inversion results of each sub-LUT, where no auxiliary data other than land cover maps were entered to reduce error transfer from additional satellite data products. It should be noted that the modeled canopy spectra were convolved with spectral response functions to match the MERIS and OLCI bands.

Table 4. Input parameters in the PROSAIL_D and the PROSPECT_D+4-Scale models for LUT generation.

	PROSAIL_D	**PROSPECT_D+4-Scale**			
Parameter	CRO/GRA	DBF	EBF	ENF	SHR
Leaf structural parameter (N)	1.5	1.2	1.8	2.5	1.8
Leaf chlorophyll content (LCC, μg cm^{-2})	10–80, step 10	10–80, step 10	10–80, step 10	10–80, step 10	10–80, step 10
Leaf carotenoid content (C_{xc}, μg cm^{-2})	LCC/4	LCC/7	LCC/7	LCC/7	LCC/7
Equivalent water thickness (C_w, cm)	0.02	0.01	0.01	0.048	0.01
Dry matter content (C_m, g cm^{-2})	0.004	0.005	0.005	0.035	0.005
Leaf anthocyanin content (C_{anth}, μg cm^{-2})	2	1	1	1	1
Leaf brown pigment content (C_{bp})	0	0	0	0	0
leaf inclination distribution function*	[1,0], [0,−1], [0,1], [−0.35,0.15], [0,0]	—	—	—	—
Leaf area index (LAI, m^2 m^{-2})	0.25, 0.5, 0.75, 1, 1.25, 1.5, 1.75, 2, 3, 4, 5, 6, 7, 8	0.5, 1, 2, 4, 6, 8	0.5, 1, 2, 4, 6, 8	0.5, 1, 2, 4, 6, 8	0.5, 1, 2, 4, 6, 8
Hot spot parameter (S_L)	0.05	—	—	—	—
Soil reflectance (ρ_s)	As shown in Figure 2	—	—	—	—
Solar zenith angle (θ_s, °)	0–60, step 10	10–70, step 10	10–70, step 10	10–70, step 10	10–70, step 10
View zenith angle (θ_v, °)	0	0	0	0	0
Relative azimuth angle (φ, °)	0	0	0	0	0
Stand density (trees/ha)	—	1000, 2000, 3000, 4000	1000, 2000, 3000, 4000	1000, 2000, 3000, 4000, 6000, 8000, 12,000	1000, 2000, 3000, 4000
Stick height (m)	—	1, 5, 10	1, 5, 10	1, 5, 10	1, 2, 3
Crown height (m)	—	5, 10, 20	5, 10, 20	5, 10, 20	1, 2, 3
Crown radius (m)	—	0.75, 1, 1.25, 1.5	0.75, 1, 1.25, 1.5	0.5, 0.75, 1, 1.25	0.75, 1, 1.25, 1.5
Crown shape	—	Spheroid	Spheroid	Cone & cylinder	Spheroid
Clumping index (ΩE)	—	0.6, 0.9	0.6, 0.9	0.5, 0.8	0.6, 0.9
Neyman grouping	—	1, 2, 3	1, 2, 3	1, 2, 3	1, 2, 3
Needle to shoot ratio (γE)	—	1	1	1.41	1
Background composition	—	Green vegetation and soil	Green vegetation and soil	Green vegetation and soil	Dry grasses and soil

* [1,0], planophile; [0,−1], plagiophile; [0,1], extremophile; [−0.35,−0.15], spherical; [0,0], uniform.

2.4.1. Canopy Reflectance Modeling—PROSAIL_D Model

It is known that turbid medium models such as 4SAIL are a poor representation of heterogeneous and structurally complex canopies since they assume a random distribution of leaves. Thus, the 4SAIL model was run in forward mode to simulate the canopy spectra for homogenous canopies, such as CRO and GRA. At the leaf level, only LCC varied, with a range of 10–80 μg cm^{-2}. The leaf carotenoid content was set to a fixed value relative to LCC because it mainly affects the reflectance of the blue band, which was not involved in the retrieval of LCC. Leaf water and dry matter content have only marginal effects on the leaf reflectance of those bands for LCC retrieval and were set at 0.02 cm and 0.004 g cm^{-2}, respectively. At the canopy level, the leaf inclination distribution function (LIDF) was set to five commonly used types, except for the erectophile distribution because of the underestimation of LCC with the consideration of erectophile distribution [39]. LAI was set from 0.25 to 8 to model the scenarios with different levels of vegetation cover. The soil reflectance was determined by multiplying the field-measured dry and bare soil spectra by five different brightness coefficients (Figure 2). The values of the solar zenith angle were set from 0° to 60°, with a step of 10°. An LUT was then generated, which contained 25 sub-LUTs corresponding to five kinds of canopy structure and five kinds of soil background.

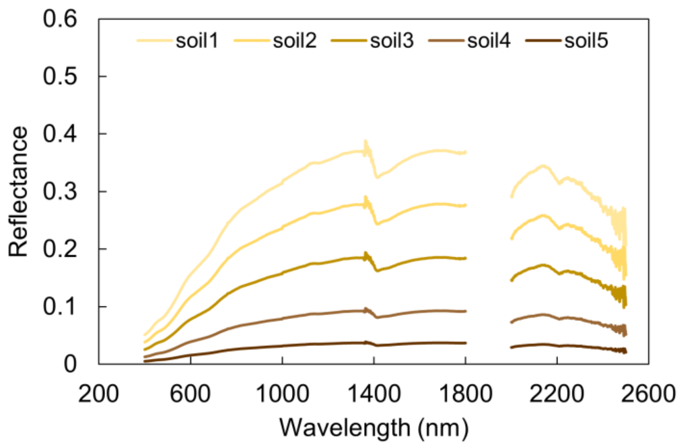

Figure 2. Soil reflectance used in the 4SAIL model. Soil1 reflectance is obtained from the field measurement. The others are the soil1 spectrum multiplied by different brightness coefficients.

2.4.2. Canopy Reflectance Modeling—PROSPECT-D and 4-Scale Models

The PROSPECT-D and 4-Scale models were selected to simulate forested and spatially clumped canopy reflectance. The 4-Scale model simulates the bidirectional reflectance distribution function (BRDF) based on canopy architecture at the following four scales: (1) tree groups, (2) tree crown geometry, (3) branches, and (4) foliage elements [49]. Firstly, leaf reflectance and transmittance were modeled using the PROSPECT-D model based on the values reported in the literature [21,50]. Then, the 4-Scale model was used to simulate canopy spectra using tree architecture, canopy structure, imaging geometry, and leaf/background properties (Table 4). The Neyman type A distribution simulates the non-random spatial distribution of trees, permitting clumping and patchiness within a forest stand [47]. The element clumping index represents vegetation clumping at scales larger than the shoot and is used to estimate radiation interception and distribution in plant canopies [51]. The simulated canopy reflectance can be representative of most forest characteristics, set according to the values in the literature [47,49,51]. Thus, modeled canopy reflectance was calculated as a linear sum of four components, as follows:

$$\rho = \rho_{PT\lambda}F_{PT} + \rho_{ZT\lambda}F_{ZT} + \rho_{PG\lambda}F_{PG} + \rho_{ZG\lambda}F_{ZG} \quad (1)$$

where ρ is the canopy reflectance, $\rho_{PT\lambda}$, $\rho_{ZT\lambda}$, $\rho_{PG\lambda}$ and $\rho_{ZG\lambda}$ are the reflectance factors from each scene component, representing sunlit vegetation, shaded vegetation, sunlit background, and shaded background, respectively, and F_{PT}, F_{ZT}, F_{PG}, and F_{ZG} represent the probabilities of a sensor view of sunlit and shaded vegetation, and sunlit and shaded background [49]. At a given viewing geometry, crown height variations impacted the modeled canopy reflectance and LCC [21,29]. The 4-Scale model was run in the forward mode to generate four LUTs used to retrieve LCC in DBF, EBF, ENF, and SHR ecosystems, respectively. Each LUT, including three sub-LUTs, was contained to consider three types of crown height.

2.4.3. Deriving Leaf Chlorophyll Content

As shown in Figure 3, an improved LUT algorithm that considers the influence of canopy structure and soil background was used to generate the GLCC dataset. MERIS and OLCI surface reflectance data were reprojected and resampled to be consistent with the MCD12Q1 product. For woody plants, each LUT, containing three sub-LUTs, corresponding to three types of crown height presented in Table 4, was used. In the processing of inversion using a physical model, the inversion results are not always unique, as different combinations of canopy and leaf parameters may produce almost similar spectra [52]. It has been indicated that using prior knowledge is an effective way to deal with this problem and facilitate LCC retrieval [5,53]. Each sub-LUT for retrieving LCC from MERIS/OLCI reflectance was optimized based on sun-view geometry that could be available from each satellite image. The root mean square error (RMSE) between MERIS/OLCI reflectance and simulated reflectance was calculated to derive the LCC value for each sub-LUT. Instead of selecting the best spectrum (case) obtained for the smallest RMSE value and its corresponding LCC as the solution, the situation of multiple best cases and the mean of their corresponding LCC values were considered. A different number of cases (the first 1, 10, 50, 100, 500, and 1000 best fits) were reviewed in the solution in retrieving LCC. It was found that the average of the best ten solutions yielded the lowest RMSE for the LCC retrieval and served as the retrieval for each sub-LUT. The final inversion result was obtained by averaging the retrievals of the three sub-LUTs while considering multiple types of crown height. The retrieval of LCC for the other woody PFTs was conducted according to the inversion process described above. It is worth noting that the four PFTs, namely WSA, SAV, GRA, and CRO, used the LUT, containing 25 sub-LUTs, established by the PROSAIL_D model. An analysis of multiple solutions (selecting the first 1, 3, 5, 8, 10, or 15 best fits) was also conducted in each sub-LUT. According to the test conducted by Qian and Liu [39], the mean of the eight best solutions yielded the best result, and the mean of the retrievals for 25 sub-LUTs was taken as the final retrieval. Multiple averages will reduce the ill-posed inversion problem and improve the robustness of the inversion method. For invalid pixels (reflectance less than 0) and non-vegetated pixels in the MERIS/OLCI data, the LCC value was set to 0.

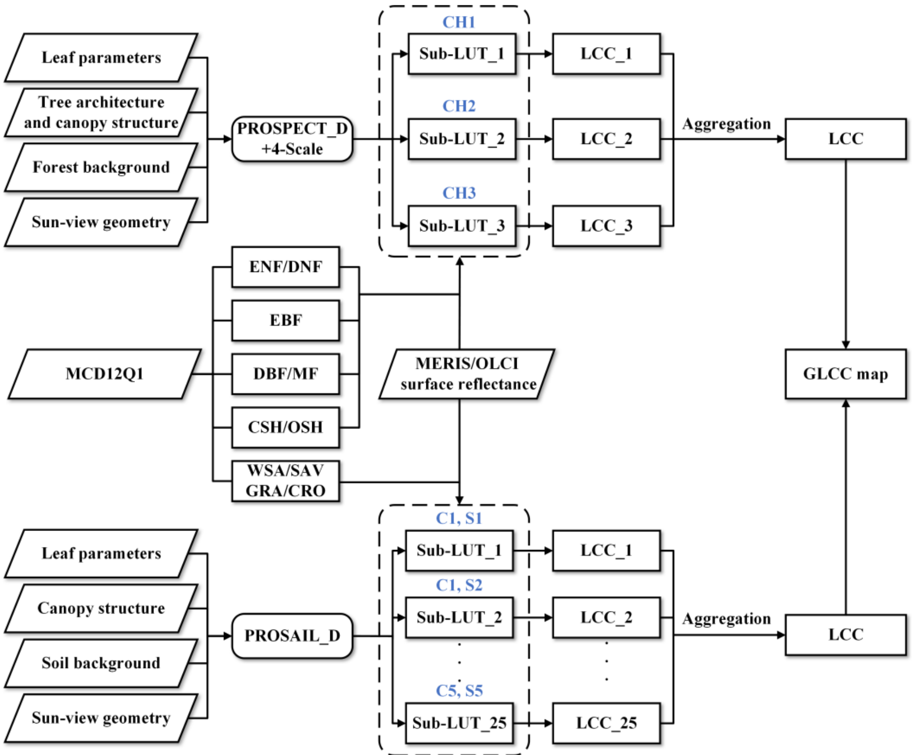

Figure 3. The flowchart of the LUT algorithm to generate GLCC dataset. CH1, CH2 and CH3 represent three types of crown height, respectively. C1 to C5 represent the canopy structures planophile, plagiophile, extremophile, spherical and uniform, respectively. S1 to S5 represent the soil backgrounds soil1, soil2, soil3, soil4 and soil5, respectively.

2.5. Validation and Evaluation of the GLCC Dataset

The GLCC dataset was validated by comparing it with the collected LCC field measurements over six PFTs in Section 2.2. In addition to field data validation, the GLCC dataset was evaluated from two aspects: first, to analyze the spatial and temporal variations in the global LCC maps; and second, to compare the new LCC dataset with the Croft MERIS LCC dataset at the cross-validation sites.

3. Results

3.1. Validation of LUT Algorithms for LCC Inversion Using the Synthetic Dataset

Randomly, 10% of the synthetic dataset was used to validate the inversion performances of the improved LUT algorithm on the five PFTs (Figure 4). All the LUT algorithms had R^2 values of higher than 0.79 and RMSE values of lower than 10.5 µg cm^{-2}. The LUT algorithm for SHR PFT achieved the highest R^2 (about 0.98) and lowest RMSE (2.8 µg cm^{-2}). Except for the DBF and EBF PFTs, the difference in LCC inversion performance of the LUT algorithm on the MERIS and OLCI synthetic datasets is negligible, indicating the applicability and effectiveness of the improved LUT algorithm for MERIS and OLCI satellite data.

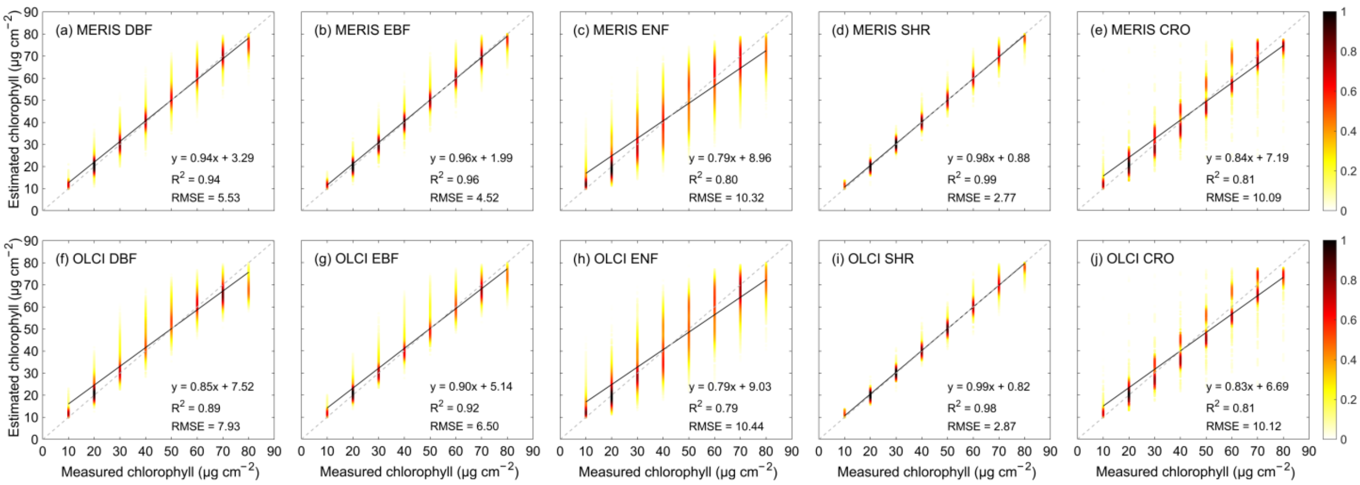

Figure 4. Performances of LCC inversion with the synthetic dataset using the LUT algorithms. (**a**–**e**) represent the performances on the MERIS synthetic dataset; (**f**–**j**) represent the performances on the OLCI synthetic dataset. Darker colors indicate higher dot density.

3.2. Validation of the GLCC Dataset Using Field Measurements

The LCC estimates against ground measurements are plotted in Figure 5 for all FPTs and Figure 6 for individual PFTs. With all PFTs combined, the GLCC dataset yielded a relatively good overall accuracy, with a coefficient of determination (R^2) value of 0.41, an RMSE value of 8.94 µg cm^{-2}, and a normalized RMSE (NRMSE=RMSE/range) value of 16.9%. In the case of considering single PFT alone, EBF performed best (R^2 = 0.61; RMSE = 8.03 µg cm^{-2}) followed by DBF (R^2 = 0.43; RMSE=8.21 µg cm^{-2}) and ENF (R^2 = 0.32; RMSE = 8.09 µg cm^{-2}). The other three PFTS showed similar levels of performance, where the RMSE values were 10.58, 10.48, and 7.37 µg cm^{-2} for CRO, GRA, and SHR, respectively. Overall, all the PFTs achieved an RMSE < 10.6 µg cm^{-2}.

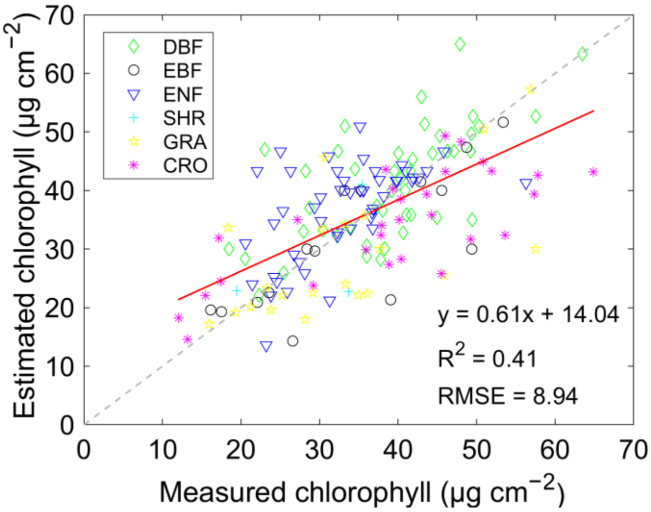

Figure 5. Validation of the GLCC dataset with field measurements for all PFTs.

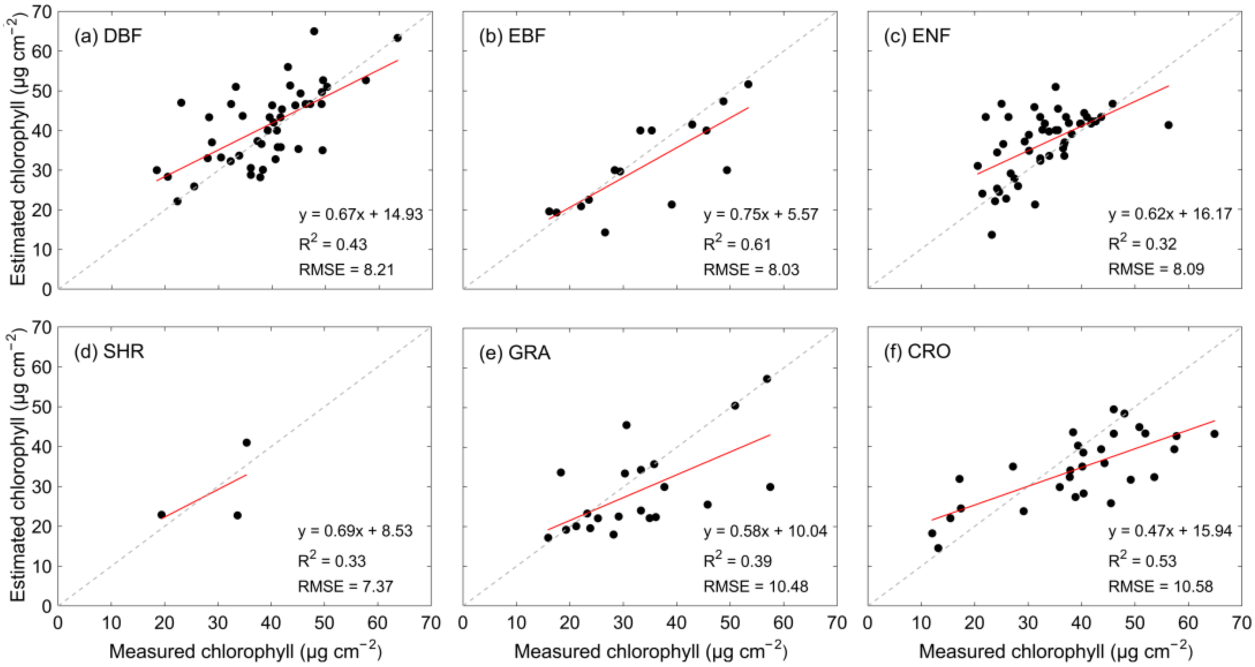

Figure 6. Validation of the GLCC dataset with field measurements for six individual PFTs.

3.3. Spatial and Temporal Trends in Global Leaf Chlorophyll Content

The annual global distribution of LCC from OLCI data is presented in Figure 7a. The tropical forests in the Congo basin, Amazon region, and Southeast Asia achieved the highest mean LCC values of higher than 40 μg cm^{-2}. DBF had relatively high values of annual mean LCC (about 40 μg cm^{-2}), while GRA had the lowest mean LCC values of lower than 30 μg cm^{-2}. The annual mean LCC values of SHR decreased with increasing latitude and did not present a fixed range of values. Figure 7b demonstrates the variation in annual mean LCC with latitude on a global scale. In general, the annual mean LCC value decreases with increasing latitude, which is in line with the general pattern of plant growth.

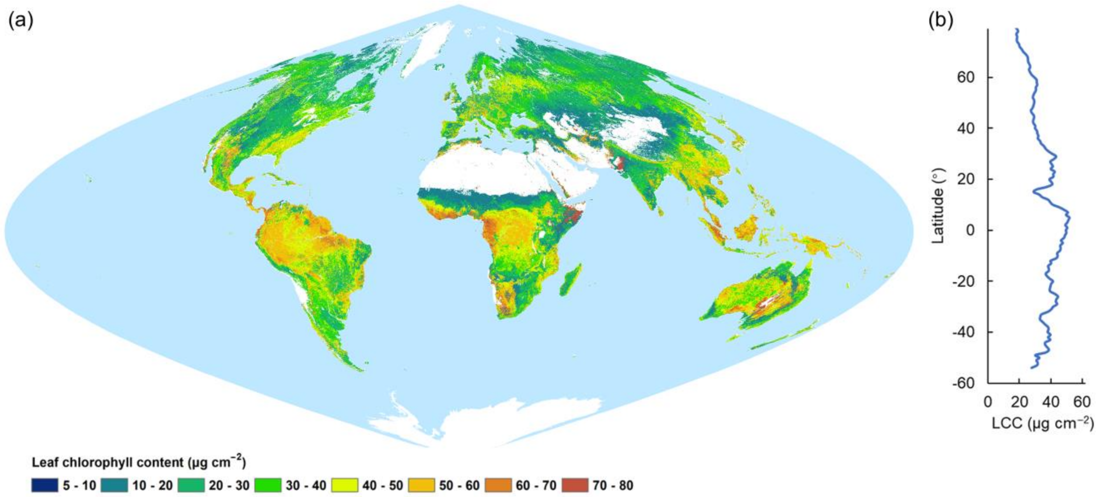

Figure 7. (**a**) The global annual mean map of GLCC in 2019 and (**b**) the mean values along latitudinal bands.

The seasonal dynamics in MERIS LCC and OLCI LCC are shown in Figure 8. The years 2009 and 2019 were divided into two seasons according to the vegetation status and climate in the northern hemisphere, i.e., a growing season from May to October and a non-growing season in the remaining six months. It can be observed that the OLCI LCC map showed a similar overall spatial distribution to the MERIS LCC map, both in the growing and the non-growing seasons, but with richer spatial details. The improved LUT algorithm can be successfully applied to OLCI data, and the dataset has the capacity to represent the LCC spatial distribution. In tropical rainforest areas, LCC remained high all year round. Distinct seasonal variations in LCC were found at the middle and high latitudes of the northern hemisphere. Boreal forests at high latitudes had a higher LCC than other PFTs, especially in the growing season. Apparent seasonal variations were also found in shrublands in South Africa and Australia.

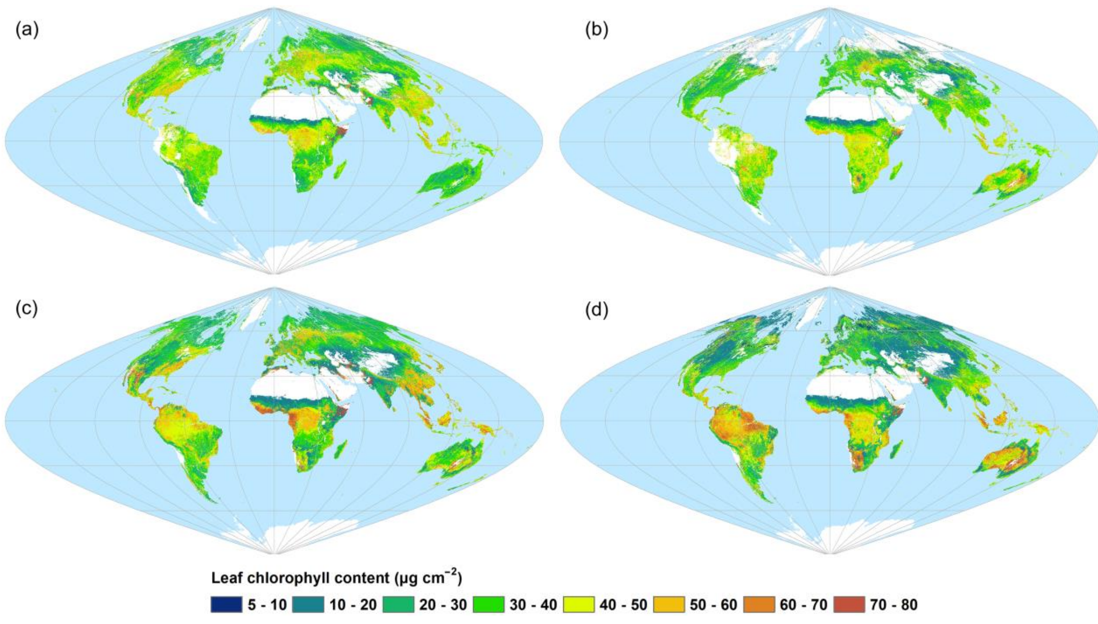

Figure 8. Spatial distribution of the mean LCC using MERIS and OLCI data in the different seasons: (**a**) and (**b**) are the mean LCC map using MERIS data in 2009 during the growing and non-growing season for the northern hemisphere, respectively; (**c**) and (**d**) are the mean LCC map using OLCI in 2019 during the growing and non-growing season for the northern hemisphere, respectively.

3.4. Comparisons of the GLCC Dataset and Croft MERIS LCC Dataset

The comparisons of GLCC with the Croft MERIS LCC dataset in different PFTs at the cross-validation sites are presented in Figure 9. The former had narrower value ranges of LCC (generally 10–80 μg cm^{-2}) than the latter (1–90 μg cm^{-2}). The GLCC had higher values than Croft MERIS LCC for DBF and ENF, with RMSE values of 15.28 and 15.44 μg cm^{-2}. The two LCC dataset values were closer for EBF and SHR, with RMSE values of 12.11 and 11.78 μg cm^{-2}. The correlation between GLCC and Croft MERIS LCC was very poor for GRA and CRO, with an $R^2 < 0.05$ and RMSE close to 17 μg cm^{-2}. For GRA, the poor correlation was because GLCC had lower values than Croft MERIS LCC, while for CRO, it was attributed to the high-density range of GLCC values (20–50 μg cm^{-2}) corresponding to an extensive range of Croft MERIS LCC values (12–60 μg cm^{-2}). In general, the GLCC using the improved LUT method was found to have an acceptable correlation with the Croft MERIS LCC, with an overall accuracy of $R^2 = 0.21$, RMSE = 15.62 μg cm^{-2}.

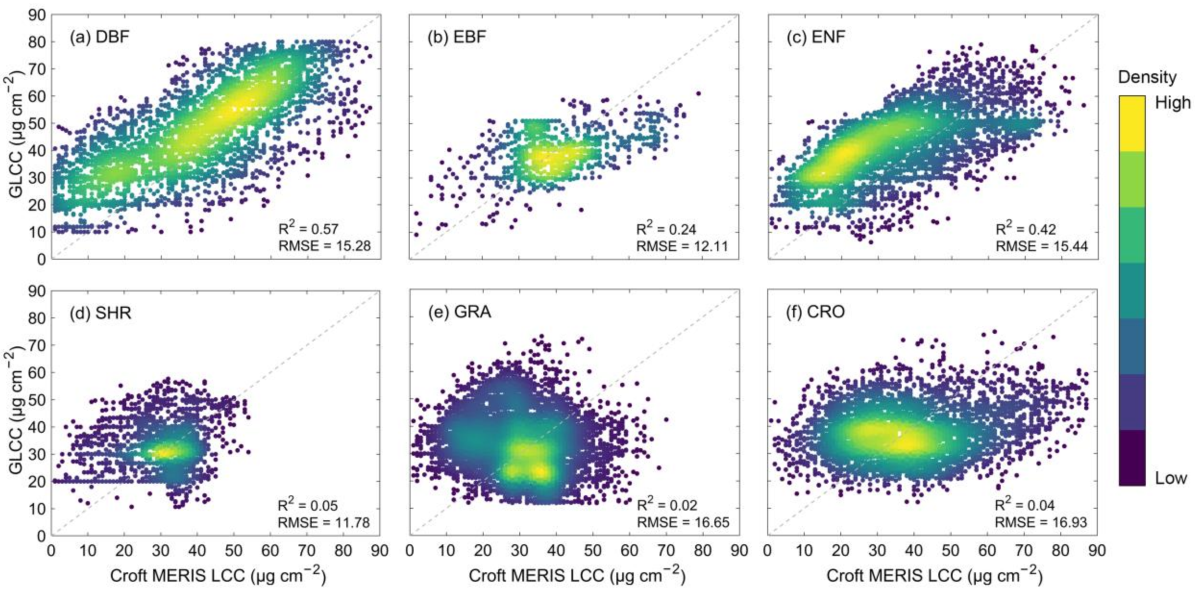

Figure 9. Comparisons of GLCC and Croft MERIS LCC in six different PFTs at the cross-validation sites.

Figure 10 shows the seasonal variations in the two LCC datasets for six different PFTs across the northern hemisphere. The two LCC datasets had the most stable seasonal variations in SHR, with the LCC value range of 20 to 40 μg cm^{-2} all year round. The GLCC presented a slight seasonal variation in comparison with Croft MERIS LCC. The GLCC seasonal trajectories in EBF were relatively consistent across the year, while the Croft MERIS LCC values varied enormously and had chaotic seasonal variations. For ENF, the two datasets had the most similar seasonal trends, while GLCC had higher LCC values than Croft MERIS LCC datasets. In DBF, the two LCC datasets presented apparent seasonal variations and the same peak, but GLCC showed higher values in winter, spring and autumn. The reason may be that the DBF validation sites at middle latitudes had a different phenology from those at high latitudes. For GRA, GLCC has a more elevated and later peak than Croft MERIS LCC, with more obvious seasonal variations. The seasonal variation of the two datasets in CRO showed opposite trends, except in summer. The GLCC had an upward trend in winter and a small peak in summer, which may be due to the lack of LCC data, as only 19 sites were involved in the statistical analysis. The results above confirmed the seasonal variation patterns of the GLCC, especially for SHR and GRA.

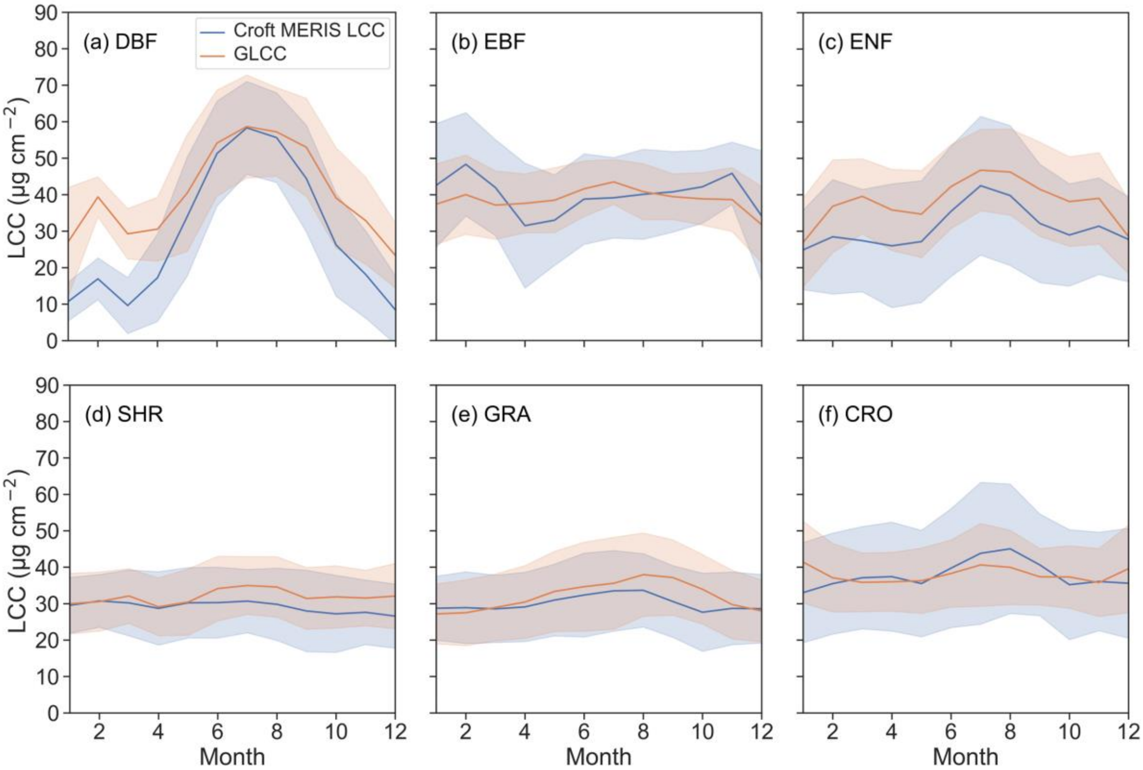

Figure 10. The mean seasonal profiles of the two LCC datasets in six different PFTs at the cross-validation sites in the northern hemisphere. The shadow areas in each subfigure represent one standard deviation.

4. Discussion

4.1. Advance in the GLCC Dataset

This study produced a global leaf chlorophyll content dataset using MERIS and OLCI satellite data spanning nearly 20 years from 2003–2012 to 2018–2020, which is of great significance for the study of global change. The overall validation results of the global GLCC dataset were considered within reasonable limits, with an overall accuracy of 8.94 μg cm^{-2} for all PFTs. The satellite-based GLCC dataset could be essential for the forthcoming ESA Sentinel Flex mission for the global mapping of vegetation fluorescence. Comparing two biophysical parameters, namely chlorophyll content and fluorescence, would provide value-added content on vegetation status.

The 4SAIL model, assuming that the canopy is composed of a homogeneous and horizontal layer of Lambert scatterers, randomly distributed in space, has limitations in simulating complex canopy structures [29,54,55]. It was used separately to simulate canopy reflectance on a global scale, leading to high LCC estimate uncertainties in forest types [22,23]. In this study, the 4-Scale model was selected to describe the heterogeneous and structural vegetation types, such as forests and shrubs.

Physically-based modeling will suffer from the ill-posed problem during LUT inversion [56]; different combinations of leaf and canopy parameters may yield similar spectra [52]. Using prior information can help solve this problem and improve the accuracy of the estimated parameters [53,57]. The assumption of a single value for some parameters may limit its applicability to larger areas. For example, the canopy structure for specific crops was usually assumed to be ellipsoidal [11,21,26], which resulted in a decrease in the inversion accuracy of nearly 2 μg cm^{-2} [39]. In addition, to obtain a good retrieval accuracy for the target parameters, the size of LUT should be considerable [20,58]. In this study, the relatively broad range of values and types were therefore selected for LCC, LAI, leaf inclination distribution function, crown density, and soil background, and multiple values were also set for parameters such as crown height, crown radius, and the clumping index to ensure that the LUT would cover as many situations as possible. On the contrary, to reduce the reduction in computational efficiency and possible decrease in the inversion accuracy caused by the redundancy of LUT information, several parameters (C_m, C_w, etc.) affecting the bands that are insensitive to LCC were set to fixed values [21,59,60].

In the inversion process, in addition to utilizing the LCC corresponding to the best-fitting spectra (with minimum RMSE as the cost function), we examined the mean of the first multiple best solutions. The strategy of multiple averaging would smooth any exceptionally high or low values; thus, seasonal variations of LCC can be better captured for vegetation types with less pronounced seasonal variations, such as EBF and SHR, by comparison with Croft MERIS LCC (Figure 10). These findings confirmed that utilizing multiple solutions results in a more robust retrieval accuracy [61–64].

4.2. Uncertainty in the GLCC Dataset

The limitations and uncertainties in the dataset are the results of factors related to the data used, the model itself, and the validation process. As only MERIS and OLCI surface reflectance and the MCD12Q1 land cover type were involved in generating LCC, the accuracy of the GLCC dataset is entirely dependent on the satellite data without considering the algorithm accuracy. These satellite products were developed by different initiatives with different objectives. ESA land cover products, such as CCI land cover and the newly released WorldCover product, could be better for LCC retrievals using the MERIS and Sentinel-3 satellite in terms of ESA standards. Uncertainties in MERIS and OLCI surface reflectance products may arise from radiometric, geometric, and BRDF corrections, as well as atmospheric corrections [65]. In addition, a pixel at a 300 m or 500 m resolution could be affected by pixel heterogeneity, leading to spatial heterogeneity in the vegetation parameter products obtained from the inversion as well [19]. The effect of pixel heterogeneity on the LUT inversion of LCC can be further evaluated by applying ESA 10 m WorldCover map.

The vegetation canopy structure and soil background are two parameters attracting the most attention in this study. LAI parameters, which can represent vegetation cover to some extent, should also be considered. Since adding an uncertain input would bring extra uncertainty in the retrieval of LCC, the LAI satellite dataset was not introduced in this study. However, the availability of a high-precision LAI dataset in the future may contribute to improving the LCC inversion accuracy [66]. Numerous studies have shown that due to the interference of soil background, the retrieval accuracy of LCC is low under sparse vegetation [5,21,26,67]. How to eliminate the influence of soil background and improve the retrieval accuracy of LCC under sparse vegetation with remote sensing is an urgent scientific question worthy of in-depth investigation [68]. The step-based sampling of LCC was chosen when generating LUT, which may lead to substantial gaps in the sampling and biased accuracy results. A normal distribution or a uniform distribution can be used to avoid these gaps. In addition, some biochemical and structural parameters were fixed as constants according to the PFT separately, which has a certain level of influence on the simulation of canopy reflectance. Since remote sensing inversion based on a physical model is an ill-posed problem, a trade-off between the universality and computational efficiency of the model and the accuracy of model inversion should be considered [22]. Hybrid models, which blend the physical foundation from radiative transfer models with the flexibility of machine learning regression algorithms, can be a fast and efficient alternative [69].

There are also limitations to the validation of the GLCC dataset. First, the lack of LCC field measurements with seasonal variations across different PFTs resulted in insufficient validation on a global scale. For example, the data are not discrete enough to result in low R^2 values due to the small standard deviation of the field LCC data in ENF and SHR PFTs (Table 3, Figure 6c,d). Despite the small amount of sampling data, satellite observations within ±7-day intervals were extracted for ground validation to avoid the retrieval accuracy being affected by the mismatch of the sampling date and the image capture date [52]. Second, the LCC validation across different PFTs was performed using data from independent field campaigns. Nevertheless, the number of measurements, the measuring position of the leaf, and the details of chlorophyll extraction are important. Although they have all been adequately validated individually, they may still introduce some uncertainty in the validation by putting them together in a natural way. Third, the scale mismatch between MERIS/OLCI and the field measurement did impact our results. Although we paid attention to the spatial homogeneity of the field sites and tried to select areas with homogeneity within 500 m, the scale problem still exists. In future, ground measurements should be upscaled using high-resolution data and then used to validate the LCC dataset [22,70].

5. Conclusions

This study generated a new global LCC dataset based on MERIS and OLCI data using an improved LUT method, considering the influence of canopy structure and soil background. For grasslands and crops, an LUT, including 25 sub-LUTs, was generated using the PROSAIL_D model. The final LCC retrievals are the mean values of the 25 sub-LUTs. For forests and shrubs, four LUTs were constructed using PROSPECT-D and 4-Scale models, applicable for evergreen needleleaf forest, evergreen broadleaf forest, deciduous broadleaf forest, and shrubs, respectively. Each LUT contains three sub-LUTs, and the final inversion result is their average value. The LUT algorithm was tested using the simulated spectra, which yielded an R^2 value higher than 0.79 and an RMSE value lower than 10.5 $\mu g\ cm^{-2}$. The global GLCC dataset was validated and evaluated by comparing it with collected field measurements and the existing LCC dataset. The GLCC dataset showed good relationships with ground measurements, with an overall accuracy of $R^2 = 0.41$ and RMSE = 8.94 $\mu g\ cm^{-2}$, and presented acceptable consistency with the existing MERIS LCC dataset. The global 7-day LCC data at a 500 m resolution from 2003–2012 to 2018–2020 provide essential information for the analysis of vegetation physiological dynamics and for carbon cycle modeling with global change.

Author Contributions: Conceptualization, L.L.; methodology, X.Q. and X.Z.; software, X.Q., X.C., and S.C.; validation, X.Q.; formal analysis, X.Q.; investigation, X.Q. and Q.S.; resources, L.L.; data curation, X.Q.; writing—original draft preparation, X.Q.; writing—review and editing, L.L. All authors have read and agreed to the published version of the manuscript.

Funding: This research was funded by the National Natural Science Foundation of China, grant number 42201383, the Innovative Research Program of the International Research Center of Big Data for Sustainable Development Goals, grant number CBAS2022IRP01, the Open Fund of State Key Laboratory of Remote Sensing Science, grant number OFSLRSS202216, and the Natural Science Research Start-up Foundation of Recruiting Talents of Nanjing University of Posts and Telecommunications, grant number NY221145.

Institutional Review Board Statement: Not applicable.

Informed Consent Statement: Not applicable.

Data Availability Statement: The global 7-day leaf chlorophyll content data at a 500 m resolution from 2003–2012 to 2018–2020 are free to access at https://doi.org/10.25452/figshare.plus.20439351.

Acknowledgments: The authors thank the authors who published the field measurement data cited in this paper, and Holly Croft for providing the published field data collection. The authors appreciate the field measurement data provided by the Center for Advanced Land Management Information Technologies (CALMIT), the University of Nebraska–Lincoln, and the National Science Foundation's National Ecological Observatory Network (NEON). The authors thank Jianhua Yang and Dong Li for their help with data processing.

Conflicts of Interest: The authors declare no conflict of interest.

References

1. Badgley, G.; Field, C.B.; Berry, J.A. Canopy near-infrared reflectance and terrestrial photosynthesis. *Sci. Adv.* **2017**, *3*, e1602244. [CrossRef]
2. Xiao, J.; Chevallier, F.; Gomez, C.; Guanter, L.; Hicke, J.A.; Huete, A.R.; Ichii, K.; Ni, W.; Pang, Y.; Rahman, A.F.; et al. Remote sensing of the terrestrial carbon cycle: A review of advances over 50 years. *Remote Sens. Environ.* **2019**, *233*, 111383. [CrossRef]
3. Ryu, Y.; Berry, J.A.; Baldocchi, D.D. What is global photosynthesis? History, uncertainties and opportunities. *Remote Sens. Environ.* **2019**, *223*, 95–114. [CrossRef]
4. Gitelson, A.; Gritz, Y.; Merzlyak, M.N. Relationships between leaf chlorophyll content and spectral reflectance and algorithms for non-destructive chlorophyll assessment in higher plant leaves. *J. Plant Physiol.* **2003**, *160*, 271–282. [CrossRef] [PubMed]
5. Li, Y.; Ma, Q.; Chen, J.M.; Croft, H.; Luo, X.; Zheng, T.; Rogers, C.; Liu, J. Fine-scale leaf chlorophyll distribution across a deciduous forest through two-step model inversion from Sentinel-2 data. *Remote Sens. Environ.* **2021**, *264*, 112618. [CrossRef]
6. Croft, H.; Chen, J.; Luo, X.; Bartlett, P.; Chen, B.; Staebler, R.M. Leaf chlorophyll content as a proxy for leaf photosynthetic capacity. *Glob. Change Biol.* **2017**, *23*, 3513–3524. [CrossRef] [PubMed]
7. Qian, X.; Liu, L.; Croft, H.; Chen, J.M. Relationship between leaf maximum carboxylation rate and chlorophyll content preserved across 13 species. *J. Geophys. Res. Biogeosci.* **2021**, *126*, e2020JG006076. [CrossRef]
8. Wang, S.; Li, Y.; Ju, W.; Chen, B.; Chen, J.; Croft, H.; Mickler, R.A.; Yang, F. Estimation of leaf photosynthetic capacity from leaf chlorophyll content and leaf age in a subtropical evergreen coniferous plantation. *J. Geophys. Res. Biogeosci.* **2020**, *125*, e2019JG005020. [CrossRef]
9. Lu, X.; Ju, W.; Li, J.; Croft, H.; Chen, J.M.; Luo, Y.; Yu, H.; Hu, H. Maximum carboxylation rate estimation with chlorophyll content as a proxy of rubisco content. *J. Geophys. Res. Biogeosci.* **2020**, *125*, e2020JG005748. [CrossRef]
10. Li, J.; Lu, X.; Ju, W.; Li, J.; Zhu, S.; Zhou, Y. Seasonal changes of leaf chlorophyll content as a proxy of photosynthetic capacity in winter wheat and paddy rice. *Ecol. Indic.* **2022**, *140*, 109018. [CrossRef]
11. Jay, S.; Maupas, F.; Bendoula, R.; Gorretta, N. Retrieving LAI, chlorophyll and nitrogen contents in sugar beet crops from multi-angular optical remote sensing: Comparison of vegetation indices and PROSAIL inversion for field phenotyping. *Field Crops Res.* **2017**, *210*, 33–46. [CrossRef]
12. Kira, O.; Linker, R.; Gitelson, A. Non-destructive estimation of foliar chlorophyll and carotenoid contents: Focus on informative spectral bands. *Int. J. Appl. Earth Obs. Geoinf.* **2015**, *38*, 251–260. [CrossRef]
13. Qian, B.; Ye, H.; Huang, W.; Xie, Q.; Pan, Y.; Xing, N.; Ren, Y.; Guo, A.; Jiao, Q.; Lan, Y. A sentinel-2-based triangular vegetation index for chlorophyll content estimation. *Agric. For. Meteorol.* **2022**, *322*, 109000. [CrossRef]
14. Zhang, Y.; Hui, J.; Qin, Q.; Sun, Y.; Zhang, T.; Sun, H.; Li, M. Transfer-learning-based approach for leaf chlorophyll content estimation of winter wheat from hyperspectral data. *Remote Sens. Environ.* **2021**, *267*, 112724. [CrossRef]
15. Jiang, X.; Zhen, J.; Miao, J.; Zhao, D.; Shen, Z.; Jiang, J.; Gao, C.; Wu, G.; Wang, J. Newly-developed three-band hyperspectral vegetation index for estimating leaf relative chlorophyll content of mangrove under different severities of pest and disease. *Ecol. Indic.* **2022**, *140*, 108978. [CrossRef]
16. Houborg, R.; Anderson, M.C.; Daughtry, C.S.T.; Kustas, W.P.; Rodell, M. Using leaf chlorophyll to parameterize light-use-efficiency within a thermal-based carbon, water and energy exchange model. *Remote Sens. Environ.* **2011**, *115*, 1694–1705. [CrossRef]
17. Luo, X.; Croft, H.; Chen, J.M.; He, L.; Keenan, T.F. Improved estimates of global terrestrial photosynthesis using information on leaf chlorophyll content. *Glob. Change Biol.* **2019**, *25*, 2499–2514. [CrossRef]
18. Piao, S.; Wang, X.; Park, T.; Chen, C.; Lian, X.; He, Y.; Bjerke, J.W.; Chen, A.; Ciais, P.; Tømmervik, H. Characteristics, drivers and feedbacks of global greening. *Nat. Rev. Earth Environ.* **2020**, *1*, 14–27. [CrossRef]
19. Croft, H.; Chen, J.M.; Zhang, Y.; Simic, A. Modelling leaf chlorophyll content in broadleaf and needle leaf canopies from ground, CASI, Landsat TM 5 and MERIS reflectance data. *Remote Sens. Environ.* **2013**, *133*, 128–140. [CrossRef]
20. Darvishzadeh, R.; Skidmore, A.; Abdullah, H.; Cherenet, E.; Ali, A.; Wang, T.; Nieuwenhuis, W.; Heurich, M.; Vrieling, A.; O'Connor, B. Mapping leaf chlorophyll content from Sentinel-2 and RapidEye data in spruce stands using the invertible forest reflectance model. *Int. J. Appl. Earth Obs. Geoinf.* **2019**, *79*, 58–70. [CrossRef]
21. Croft, H.; Chen, J.M.; Wang, R.; Mo, G.; Luo, S.; Luo, X.; He, L.; Gonsamo, A.; Arabian, J.; Zhang, Y. The global distribution of leaf chlorophyll content. *Remote Sens. Environ.* **2020**, *236*, 111479. [CrossRef]
22. Xu, M.; Liu, R.; Chen, J.M.; Shang, R.; Liu, Y.; Qi, L.; Croft, H.; Ju, W.; Zhang, Y.; He, Y. Retrieving global leaf chlorophyll content from MERIS data using a neural network method. *ISPRS J. Photogramm. Remote Sens.* **2022**, *192*, 66–82. [CrossRef]
23. Xu, M.; Liu, R.; Chen, J.M.; Liu, Y.; Wolanin, A.; Croft, H.; He, L.; Shang, R.; Ju, W.; Zhang, Y. A 21-Year Time Series of Global Leaf Chlorophyll Content Maps from MODIS Imagery. *IEEE Trans. Geosci. Remote Sens.* **2022**, *60*, 4413513. [CrossRef]
24. Jay, S.; Gorretta, N.; Morel, J.; Maupas, F.; Bendoula, R.; Rabatel, G.; Dutartre, D.; Comar, A.; Baret, F. Estimating leaf chlorophyll content in sugar beet canopies using millimeter- to centimeter-scale reflectance imagery. *Remote Sens. Environ.* **2017**, *198*, 173–186. [CrossRef]
25. Li, D.; Chen, J.M.; Zhang, X.; Yan, Y.; Zhu, J.; Zheng, H.; Zhou, K.; Yao, X.; Tian, Y.; Zhu, Y. Improved estimation of leaf chlorophyll content of row crops from canopy reflectance spectra through minimizing canopy structural effects and optimizing off-noon observation time. *Remote Sens. Environ.* **2020**, *248*, 111985. [CrossRef]
26. Xu, M.; Liu, R.; Chen, J.M.; Liu, Y.; Shang, R.; Ju, W.; Wu, C.; Huang, W. Retrieving leaf chlorophyll content using a matrix-based vegetation index combination approach. *Remote Sens. Environ.* **2019**, *224*, 60–73. [CrossRef]

27. Houborg, R.; Anderson, M.; Daughtry, C. Utility of an image-based canopy reflectance modeling tool for remote estimation of LAI and leaf chlorophyll content at the field scale. *Remote Sens. Environ.* **2009**, *113*, 259–274. [CrossRef]
28. Zarco-Tejada, P.J.; Berjón, A.; López-Lozano, R.; Miller, J.R.; Martín, P.; Cachorro, V.; González, M.R.; De Frutos, A. Assessing vineyard condition with hyperspectral indices: Leaf and canopy reflectance simulation in a row-structured discontinuous canopy. *Remote Sens. Environ.* **2005**, *99*, 271–287. [CrossRef]
29. Zhang, Y.; Chen, J.M.; Miller, J.R.; Noland, T.L. Leaf chlorophyll content retrieval from airborne hyperspectral remote sensing imagery. *Remote Sens. Environ.* **2008**, *112*, 3234–3247. [CrossRef]
30. Verrelst, J.; Camps-Valls, G.; Muñoz-Marí, J.; Rivera, J.P.; Veroustraete, F.; Clevers, J.G.P.W.; Moreno, J. Optical remote sensing and the retrieval of terrestrial vegetation bio-geophysical properties–A review. *ISPRS J. Photogramm. Remote Sens.* **2015**, *108*, 273–290. [CrossRef]
31. Haboudane, D.; Miller, J.R.; Tremblay, N.; Zarco-Tejada, P.J.; Dextraze, L. Integrated narrow-band vegetation indices for prediction of crop chlorophyll content for application to precision agriculture. *Remote Sens. Environ.* **2002**, *81*, 416–426. [CrossRef]
32. Wu, C.; Niu, Z.; Tang, Q.; Huang, W. Estimating chlorophyll content from hyperspectral vegetation indices: Modeling and validation. *Agric. For. Meteorol.* **2008**, *148*, 1230–1241. [CrossRef]
33. Croft, H.; Chen, J.M.; Zhang, Y. The applicability of empirical vegetation indices for determining leaf chlorophyll content over different leaf and canopy structures. *Ecol. Complex.* **2014**, *17*, 119–130. [CrossRef]
34. Sims, D.A.; Gamon, J.A. Relationships between leaf pigment content and spectral reflectance across a wide range of species, leaf structures and developmental stages. *Remote Sens. Environ.* **2002**, *81*, 337–354. [CrossRef]
35. Daughtry, C.S.T.; Walthall, C.L.; Kim, M.S.; De Colstoun, E.B.; McMurtrey Iii, J.E. Estimating corn leaf chlorophyll concentration from leaf and canopy reflectance. *Remote Sens. Environ.* **2000**, *74*, 229–239. [CrossRef]
36. Yin, G.; Verger, A.; Descals, A.; Filella, I.; Peñuelas, J. A broadband green-red vegetation index for monitoring gross primary production phenology. *J. Remote Sens.* **2022**, *2022*, 9764982. [CrossRef]
37. Croft, H.; Chen, J.M. Leaf pigment content. In *Comprehensive Remote Sensing*; Elsevier: Amsterdam, The Netherlands, 2017; pp. 117–142.
38. Sun, J.; Shi, S.; Yang, J.; Du, L.; Gong, W.; Chen, B.; Song, S. Analyzing the performance of PROSPECT model inversion based on different spectral information for leaf biochemical properties retrieval. *ISPRS J. Photogramm. Remote Sens.* **2018**, *135*, 74–83. [CrossRef]
39. Qian, X.; Liu, L. Retrieving crop leaf chlorophyll content using an improved look-up-table approach by combining multiple canopy structures and soil backgrounds. *Remote Sens.* **2020**, *12*, 2139. [CrossRef]
40. Curran, P.J.; Steele, C.M. MERIS: The re-branding of an ocean sensor. *Int. J. Remote Sens.* **2005**, *26*, 1781–1798. [CrossRef]
41. Keller, M.; Schimel, D.S.; Hargrove, W.W.; Hoffman, F.M. A continental strategy for the National Ecological Observatory Network. *Ecol. Soc. Am.* **2008**, *6*, 282–284. [CrossRef]
42. Scholl, V.M.; Cattau, M.E.; Joseph, M.B.; Balch, J.K. Integrating National Ecological Observatory Network (NEON) airborne remote sensing and in-situ data for optimal tree species classification. *Remote Sens.* **2020**, *12*, 1414. [CrossRef]
43. Simic, A.; Chen, J.M.; Noland, T.L. Retrieval of forest chlorophyll content using canopy structure parameters derived from multi-angle data: The measurement concept of combining nadir hyperspectral and off-nadir multispectral data. *Int. J. Remote Sens.* **2011**, *32*, 5621–5644. [CrossRef]
44. Zhang, Y.; Chen, J.M.; Thomas, S.C. Retrieving seasonal variation in chlorophyll content of overstory and understory sugar maple leaves from leaf-level hyperspectral data. *Can. J. Remote Sens.* **2007**, *33*, 406–415. [CrossRef]
45. NEON (National Ecological Observatory Network). *Plant Foliar Traits (DP1.10026.001)*; NEON (National Ecological Observatory Network): Fitchburg, MA, USA, 2022. [CrossRef]
46. Verhoef, W.; Jia, L.; Xiao, Q.; Su, Z. Unified optical-thermal four-stream radiative transfer theory for homogeneous vegetation canopies. *IEEE Trans. Geosci. Remote Sens.* **2007**, *45*, 1808–1822. [CrossRef]
47. Chen, J.M.; Leblanc, S.G. A four-scale bidirectional reflectance model based on canopy architecture. *IEEE Trans. Geosci. Remote Sens.* **1997**, *35*, 1316–1337. [CrossRef]
48. Féret, J.B.; Gitelson, A.A.; Noble, S.D.; Jacquemoud, S. PROSPECT-D: Towards modeling leaf optical properties through a complete lifecycle. *Remote Sens. Environ.* **2017**, *193*, 204–215. [CrossRef]
49. Chen, J.M.; Leblanc, S.G. Multiple-scattering scheme useful for geometric optical modeling. *IEEE Trans. Geosci. Remote Sens.* **2001**, *39*, 1061–1071. [CrossRef]
50. Sun, Q.; Jiao, Q.; Liu, L.; Liu, X.; Qian, X.; Zhang, X.; Zhang, B. Improving the retrieval of forest canopy chlorophyll content from MERIS dataset by introducing the vegetation clumping Index. *IEEE J. Sel. Top. Appl. Earth Obs. Remote Sens.* **2021**, *14*, 5515–5528. [CrossRef]
51. Chen, J.M.; Menges, C.H.; Leblanc, S.G. Global mapping of foliage clumping index using multi-angular satellite data. *Remote Sens. Environ.* **2005**, *97*, 447–457. [CrossRef]
52. Si, Y.; Schlerf, M.; Zurita-Milla, R.; Skidmore, A.; Wang, T. Mapping spatio-temporal variation of grassland quantity and quality using MERIS data and the PROSAIL model. *Remote Sens. Environ.* **2012**, *121*, 415–425. [CrossRef]
53. Sun, J.; Shi, S.; Wang, L.; Li, H.; Wang, S.; Gong, W.; Tagesson, T. Optimizing LUT-based inversion of leaf chlorophyll from hyperspectral lidar data: Role of cost functions and regulation strategies. *Int. J. Appl. Earth Obs. Geoinf.* **2021**, *105*, 102602. [CrossRef]

54. Gastellu-Etchegorry, J.; Gascon, F.; Esteve, P. An interpolation procedure for generalizing a look-up table inversion method. *Remote Sens. Environ.* **2003**, *87*, 55–71. [CrossRef]
55. Verhoef, W. Light scattering by leaf layers with application to canopy reflectance modeling: The SAIL model. *Remote Sens. Environ.* **1984**, *16*, 125–141. [CrossRef]
56. Atzberger, C. Object-based retrieval of biophysical canopy variables using artificial neural nets and radiative transfer models. *Remote Sens. Environ.* **2004**, *93*, 53–67. [CrossRef]
57. Combal, B.; Baret, F.; Weiss, M.; Trubuil, A.; Mace, D.; Pragnere, A.; Myneni, R.; Knyazikhin, Y.; Wang, L. Retrieval of canopy biophysical variables from bidirectional reflectance—Using prior information to solve the ill-posed inverse problem. *Remote Sens. Environ.* **2003**, *84*, 1–15. [CrossRef]
58. Atzberger, C.; Darvishzadeh, R.; Immitzer, M.; Schlerf, M.; Skidmore, A.; Le Maire, G. Comparative analysis of different retrieval methods for mapping grassland leaf area index using airborne imaging spectroscopy. *Int. J. Appl. Earth Obs. Geoinf.* **2015**, *43*, 19–31. [CrossRef]
59. Zhang, H.; Li, J.; Liu, Q.; Lin, S.; Huete, A.; Liu, L.; Croft, H.; Clevers, J.G.P.W.; Zeng, Y.; Wang, X.; et al. A novel red-edge spectral index for retrieving the leaf chlorophyll content. *Methods Ecol. Evol.* **2022**, *13*, 2771–2787. [CrossRef]
60. Roosjen, P.P.J.; Brede, B.; Suomalainen, J.M.; Bartholomeus, H.M.; Kooistra, L.; Clevers, J.G.P.W. Improved estimation of leaf area index and leaf chlorophyll content of a potato crop using multi-angle spectral data–potential of unmanned aerial vehicle imagery. *Int. J. Appl. Earth Obs. Geoinf.* **2018**, *66*, 14–26. [CrossRef]
61. Atzberger, C.; Darvishzadeh, R.; Schlerf, M.; Le Maire, G. Suitability and adaptation of PROSAIL radiative transfer model for hyperspectral grassland studies. *Remote Sens. Lett.* **2013**, *4*, 55–64. [CrossRef]
62. Darvishzadeh, R.; Matkan, A.A.; Ahangar, A.D. Inversion of a radiative transfer model for estimation of rice canopy chlorophyll content using a lookup-table approach. *IEEE J. Sel. Top. Appl. Earth Obs. Remote Sens.* **2012**, *5*, 1222–1230. [CrossRef]
63. Darvishzadeh, R.; Skidmore, A.; Schlerf, M.; Atzberger, C. Inversion of a radiative transfer model for estimating vegetation LAI and chlorophyll in a heterogeneous grassland. *Remote Sens. Environ.* **2008**, *112*, 2592–2604. [CrossRef]
64. Darvishzadeh, R.; Atzberger, C.; Skidmore, A.; Schlerf, M. Mapping grassland leaf area index with airborne hyperspectral imagery: A comparison study of statistical approaches and inversion of radiative transfer models. *ISPRS J. Photogramm. Remote Sens.* **2011**, *66*, 894–906. [CrossRef]
65. Garrigues, S.; Lacaze, R.; Baret, F.J.T.M.; Morisette, J.T.; Weiss, M.; Nickeson, J.E.; Fernandes, R.; Plummer, S.; Shabanov, N.V.; Myneni, R.B. Validation and intercomparison of global Leaf Area Index products derived from remote sensing data. *J. Geophys. Res. Biogeosci.* **2008**, *113*, 2–9. [CrossRef]
66. Tang, H.; Dubayah, R.; Brolly, M.; Ganguly, S.; Zhang, G. Large-scale retrieval of leaf area index and vertical foliage profile from the spaceborne waveform lidar (GLAS/ICESat). *Remote Sens. Environ.* **2014**, *154*, 8–18. [CrossRef]
67. Zarco-Tejada, P.J.; Hornero, A.; Beck, P.S.A.; Kattenborn, T.; Kempeneers, P.; Hernández-Clemente, R. Chlorophyll content estimation in an open-canopy conifer forest with Sentinel-2A and hyperspectral imagery in the context of forest decline. *Remote Sens. Environ.* **2019**, *223*, 320–335. [CrossRef] [PubMed]
68. Li, D.; Chen, J.M.; Yu, W.; Zheng, H.; Yao, X.; Cao, W.; Wei, D.; Xiao, C.; Zhu, Y.; Cheng, T. Assessing a soil-removed semi-empirical model for estimating leaf chlorophyll content. *Remote Sens. Environ.* **2022**, *282*, 113284. [CrossRef]
69. Reyes-Muñoz, P.; Pipia, L.; Salinero-Delgado, M.; Belda, S.; Berger, K.; Estévez, J.; Morata, M.; Rivera-Caicedo, J.P.; Verrelst, J. Quantifying Fundamental Vegetation Traits over Europe Using the Sentinel-3 OLCI Catalogue in Google Earth Engine. *Remote Sens.* **2022**, *14*, 1347. [CrossRef] [PubMed]
70. Brown, L.A.; Dash, J.; Lidón, A.L.; Lopez-Baeza, E.; Dransfeld, S. Synergetic exploitation of the Sentinel-2 missions for validating the Sentinel-3 ocean and land color instrument terrestrial chlorophyll index over a vineyard dominated mediterranean environment. *IEEE J. Sel. Top. Appl. Earth Obs. Remote Sens.* **2019**, *12*, 2244–2251. [CrossRef]